Bioconjugate Chemistry

Article

pubs.acs.org/bc

New Dioxaborolane Chemistry Enables [^{18}F]-Positron-Emitting, Fluorescent [^{18}F]-Multimodality Biomolecule Generation from the Solid Phase

Erik A. Rodriguez,[†,#] Ye Wang,[§,#] Jessica L. Crisp,[†] David R. Vera,[∥] Roger Y. Tsien,[†,‡] and Richard Ting[*,†,§]

[†]Department of Pharmacology and [∥]Department of Radiology, University of California, San Diego, La Jolla, California 92093, United States

[§]Molecular Imaging Innovations Institute (MI3), Department of Radiology, Weill Cornell Medicine, New York, New York 10065, United States

[‡]Howard Hughes Medical Institute, La Jolla, California 92093, United States

Supporting Information

ABSTRACT: New protecting group chemistry is used to greatly simplify imaging probe production. Temperature and organic solvent-sensitive biomolecules are covalently attached to a biotin-bearing dioxaborolane, which facilitates antibody immobilization on a streptavidin-agarose solid-phase support. Treatment with aqueous fluoride triggers fluoride-labeled antibody release from the solid phase, separated from unlabeled antibody, and creates [^{18}F]-trifluoroborate-antibody for positron emission tomography and near-infrared fluorescent (PET/NIRF) multimodality imaging. This dioxaborolane-fluoride reaction is bioorthogonal, does not inhibit antigen binding, and increases [^{18}F]-specific activity relative to solution-based radiosyntheses. Two applications are investigated: an anti-epithelial cell adhesion molecule (EpCAM) monoclonal antibody (mAb) that labels prostate tumors and Cetuximab, an anti-epidermal growth factor receptor (EGFR) mAb (FDA approved) that labels lung adenocarcinoma tumors. Colocalized, tumor-specific NIRF and PET imaging confirm utility of the new technology. The described chemistry should allow labeling of many commercial systems, diabodies, nanoparticles, and small molecules for dual modality imaging of many diseases.

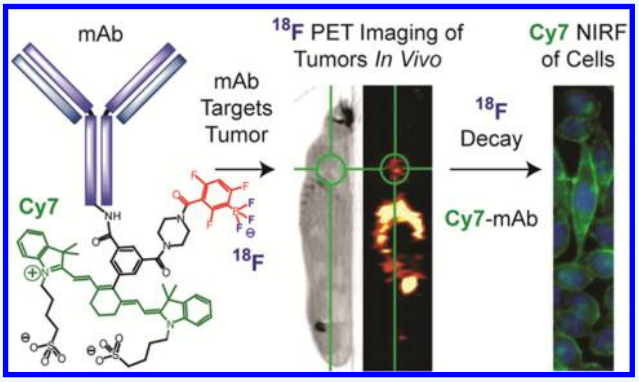

INTRODUCTION

Aryl dioxaborolanes play an important role in molecular imaging, with notable applications in peroxide sensing,[1−3] positron emission tomography,[4−6] and multimodality imaging.[7] These highly nucleophile-selective dioxaborolanes can be additionally modified for more complex application. New chemistry is described for incorporating dioxaborolanes into fluoride-reactive, chloride-ion inert, cleavable linkers. These bisfunctionalized synthons improve upon silicon-based fluoride-reactive linker technology[8,9] and have added utility in ^{18}F-PET. Cleavable linkers have application in a broad range of chemical biology applications including proteomics, imaging, and sequencing.[10]

Dioxaborolanes can be incorporated into novel immobilization chemistry to greatly simplify the generation of multimodality [^{18}F]-positron emission tomography (PET)/near-infrared fluorescent (NIRF) imaging probes. This system combines the advantages of solid-phase radiotracer generation with the clinically unique decay properties of the [^{18}F]-PET nuclide ($t_{1/2}$ = 110 min, 96.7% β^+, 0.25 MeV mean energy).[6,11] It is recognized that the [^{18}F]-fluoride reaction with a dioxaborolane is so favorable that a 5-membered-cycle is decomposed to give trifluoroborate formation. The resulting labeling strategy (Scheme S1) differs from competitive, late-stage [^{18}F]-fluoride capture technologies[12−19] because it is bioorthogonal and unique to boron.

A bioorthogonal radiolabeling strategy must occur in conditions that are not detrimental to biomolecule activity. Monoclonal antibodies (mAbs) are ideal biomolecules for testing bioorthogonality, as they are inexpensive, and have mAb-antigen specificities that are more sensitive to denaturation in organic solvents and high temperatures than small molecules. ^{18}F has a short decay half-life that does not match the long biological half-life of antibodies, resulting in imperfect, [^{18}F]-signal-to-noise at a tumor. However, a [^{18}F]-PET-mAb is not the same as a [^{18}F]-PET/NIRF-mAb. The latter has additional utility in the fluorescent mode. Multimodality imaging may compensate for a suboptimal PET image[20] since NIRF probes do not decay like

Received: March 25, 2016
Published: April 11, 2016

DOI: 10.1021/acs.bioconjchem.6b00164
Bioconjugate Chem. 2016, 27, 1390−1399

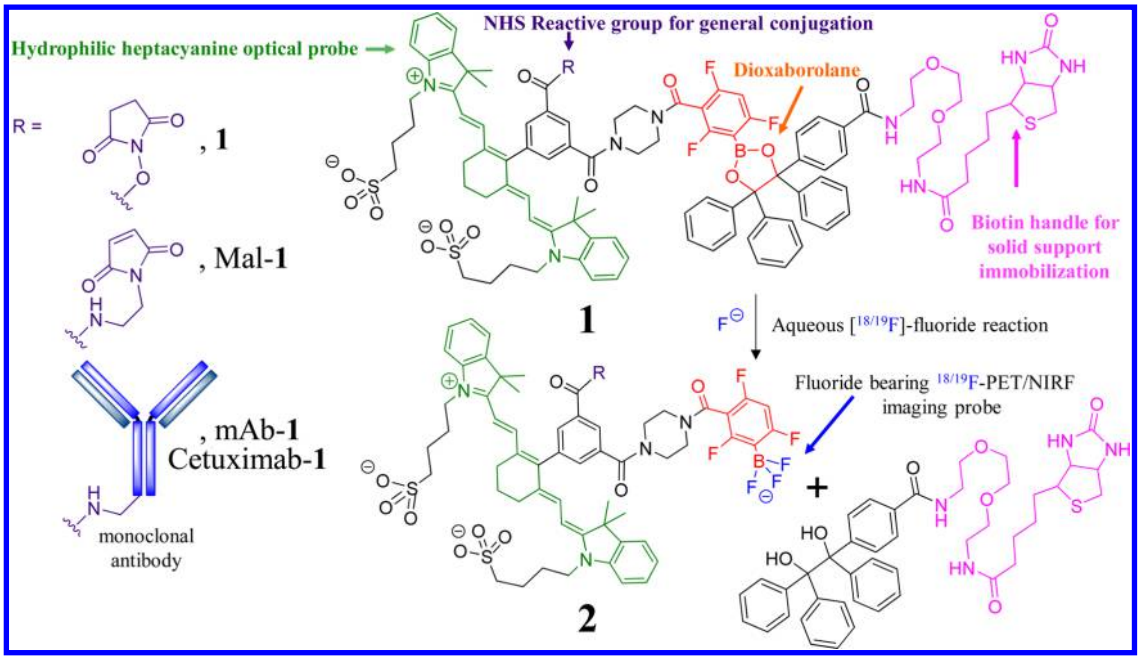

Figure 1. Chemical structure of the ^{18}F-PET/NIRF probe. The amide reactive ^{18}F-PET/NIRF precursor, **1**, the maleimide precursor, Mal-**1**, and the monoclonal antibody conjugate, mAb-**1** (EpCAM) or Cetuximab-**1** as R groups (left panel). A fluoride-labile, mAb-**1**-bearing, solid support is generated when the *N*-hydroxy succinimide ester (NHS)/maleimide precursor is reacted with mAb and then exposed to a streptavidin bearing support. mAb that is not covalently attached to **1** cannot be retained by the support and is removed with washing. Treatment of the solid support with aqueous fluoride achieves conversion of **1** into a $^{18/19}$F labeled trifluoroborate **2**, a species useful for PET/NIRF multimodality imaging and simultaneous release of ^{18}F-PET/NIRF labeled mAb-**2** from the solid support. Unreacted mAb-**1** remains bound to the support through the biotin handle on the solid-phase support (Scheme S1).

radioisotopes. For reasons like these, PET/NIRF multimodality imaging is superior to standalone SPECT, PET, and NIRF in all its facets, including depth-of-penetration, spatial, and temporal resolution.[7,21]

Hendricks et al. has set precedent by being the first group to demonstrate multimodality [^{18}F]-PET/fluorescent labeling on [^{18}F]-PET/BODIPY-labeled, systemically injected, Herceptin mAb.[15] We build on this PET/fluorescent-mAb precedent with new bioorthogonal aryl dioxaborolane chemistry that additionally incorporates a near-infrared fluorophore and novel dioxaborolane cleavable-linker technology. Fluoride-triggered dioxaborolane decomposition is so mild that mAbs can be fluoridated directly, without inhibiting antigen binding. The new technology is verified on two commercially available mAbs for imaging prostate (PC3)[22] or lung (A549) cancers in vitro and in vivo. Enough [^{18}F]-labeled mAb is generated for systemic injection in seven mice. Four mice are simultaneously [^{18}F]-PET imaged on an Inveon PET/CT (Video S1). The design of compound **1** (Figure 1, Scheme S2) centers on a dioxaborolane that is functionalized so that a boron atom serves as a fluoride-reactive, critical link between our tracer and a solid phase. We mimic the current strategy utilized in ^{99m}Tc SPECT radiosynthesis using [^{18}F]-fluoride, a clinically unique PET isotope.[23,24]

We choose to investigate a systemic mAb application due to the abundance of PET/NIRF literature on the topic.[25−27] The reported boronate chemistry is generally applicable to other biomolecules including other [^{18}F]-PET/NIRF-mAbs that can be used additionally in other nonsystemically delivered applications, like lymphatic mapping and drug delivery.[28,29]

RESULTS

Syntheses and Small Molecule Reactivity. Dioxaborolane **1** is modified at boron with both a heptamethinecyanine-NIR fluorophore and an NHS ester so that **1** can be generally applied to amine-bearing targets for multimodality imaging. Biotinylation of the dioxaborolane's 1,2-diol gives a prototype for solid-phase, streptavidin-agarose labeling. A thiol-reactive maleimide derivative of **1**, Mal-**1**, is also synthesized (Figure 1, Figures S1−S2).

Small Molecule, Solid-Phase Capture and Release. The reaction of solid-phase-bound **1** with aqueous fluoride achieves two simultaneous events: the generation of **2**, a free trifluoroborate imaging agent that can no longer bind streptavidin-agarose, and the release of **2** from the solid phase. Unreacted, non-fluoride-bearing **1** remains bound to the solid-phase, resolved from fluoride-bearing **2** (Figures S1−S4). The conversion of streptavidin-agarose bound Mal-**1** into free Mal-**2** is achieved at room temperature in 40 min with 13.4 mM HF (pH 3.0). Eluted Mal-**2** contains only 10% of the 750 nm absorbance, a majority of Mal-**1** absorbance remains bound to streptavidin-agarose as the biotinylated starting material, Mal-**1**. No Mal-**1** was detected in the eluent by HPLC (Figure S4). This reusable, dioxaborolane containing matrix can be flushed with [^{18}F]-fluoride to elute the desired radiotracer in multiple synthetic rounds.

Solid-Phase mAb Capture and Fluoride Specific Elution. The mild conditions associated with solid-phase attachment and fluoride elution encourage us to apply this chemistry to complex biological targets. Two commercially available mAbs for imaging prostate (anti-EpCAM mAb)[22] or lung (Erbitux) cancers could be labeled with 2 equiv of **1** in mild conditions (Scheme S1) to give mAb-**1** in <1 h (Figure S5). mAb-**1** is functionalized on streptavidin-agarose at 14 ± 5 pmols mAb-**1** per μL (Figure S6) and reacted with acidic fluoride to give mAb-**2** in <1 h (Figure 2). Centrifuge-based, solid-support elution of mAb-**2** is fast, separates mAb-**2** from mAb-**1**, and is

DOI: 10.1021/acs.bioconjchem.6b00164
Bioconjugate Chem. 2016, 27, 1390−1399

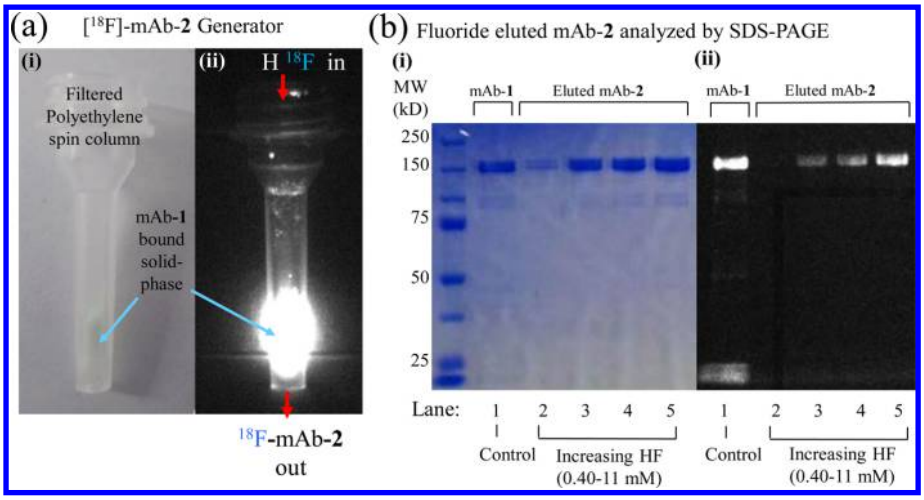

Figure 2. Validation of solid-phase, fluoride triggered mAb-**2** elution. (a) Brightfield (i) and fluorescent (ii) images of the solid-phase generator. A spin column loaded with a streptavidin-agarose that binds biotin on mAb-**1**. (b) SDS-PAGE gel of eluent generated by treating the mAb-**1**-streptavidin-agarose (a) with aqueous fluoride. (Lane 1) Control with only mAb-**1** (no streptavidin-agarose or HF). mAb-**1**-streptavidin-agarose was treated with 0.40, 1.2, 3.6, or 11 mM fluoride for 1 h (Lanes 2−5, respectively). mAb-**2** was removed by centrifugation and analyzed by SDS-PAGE. Untreated mAb-**1** (Lane 1) has a similar MW to HF treated samples (Lanes 2−5), and lacks lower MW species. Increasing quantities of mAb-**2** are released with higher concentrations of fluoride.

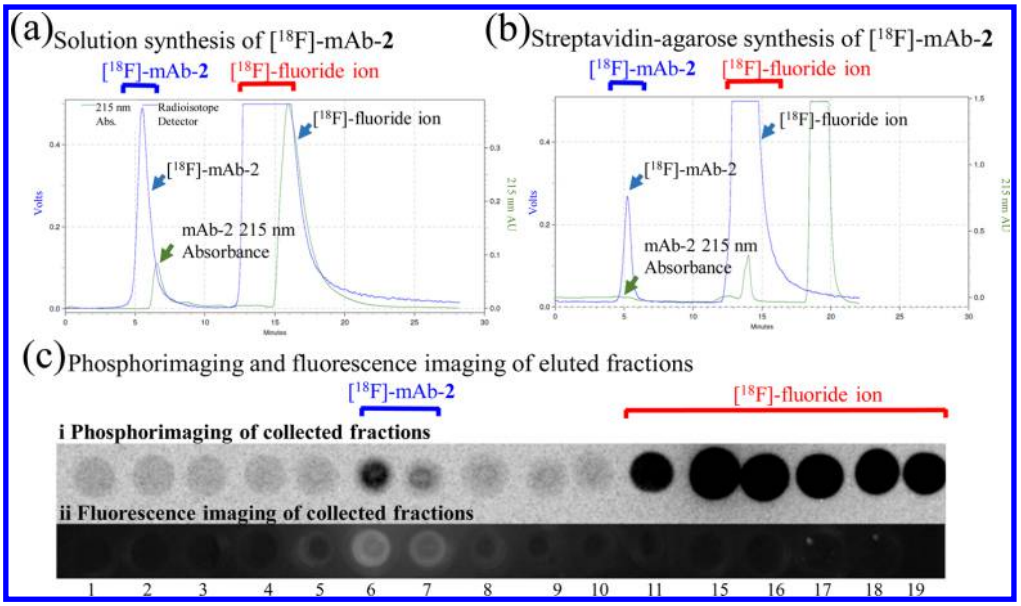

Figure 3. Radiolabeling of [^{18}F]-mAb-**2**. (a) Radioactive, SEC HPLC of [^{18}F]-mAb-**2** generated by solution fluoridation of mAb-**1** (1 h, [^{18}F]-hydrogen fluoride, pH 3). No streptavidin-agarose was utilized in this synthesis. (b) Radioactive, SEC HPLC [^{18}F]-mAb-**2** fluoride triggered elution from mAb-**1**-streptavidin-agarose. Note the 13-fold enhancement of specific activity. Elution of [^{18}F]-mAb-**2** takes 5−7 min, and is free of [^{18}F]-fluoride ion. (c) Phosphorimaging (i) and Cy7 fluorescence imaging (ii) of fractions verify SEC HPLC data. Fractions 5−7 min contain [^{18}F]-mAb-**2** and are both radioactive (i) and fluorescent (ii), indicating the successful synthesis of a dual modality, PET/NIRF imaging mAb-**2**.

superior to traditional labelings that require the separation of multiple active species. mAb-**1** bears supports to be reused in multiple radiolabelings, eliminating the need for very high radiochemical yields. Nonspecific binding is not observed (Figures S7−S9).

Radiochemistry. Radioactive [^{18}F]-fluoride (pH 3) can be used to convert mAb-**1**-bound-streptavidin-agarose into the free trifluoroborate, [^{18}F]-mAb-**2**. Starting from 29.3 mCi of [^{18}F]-sodium fluoride, the high-activity streptavidin-agarose-assisted radiolabeling has a specific activity of 160 mCi/μmol [^{18}F]-mAb-**2** (t = 82 min). Enough activity is produced for imaging four mice simultaneously in a PET/CT for up to 6 h (Video S1). To verify the successful synthesis of [^{18}F]-mAb-**2**, fractions were collected, scintillated, decayed to background, and fluorescently imaged to show that [^{18}F]-mAb-**2** elutes between 5 and 7 min in a fraction containing both [^{18}F]-radioactivity and Cy7 fluorescence (Figure 3c).

Low-Activity Radiolabelings Show a Streptavidin-Based Enhancement of Specific Activity. Low activity radiolabelings show an enhancement of [^{18}F]-mAb-**2** specific activity due to the removal of contaminating mAb and mAb-**1** from [^{18}F]-mAb-**2** by the dioxaborolane system (Scheme S1, Figures S10−S12). When 2.5 mCi doses of [^{18}F]-sodium fluoride were reacted with mAb-**1**, the greatest specific activity syntheses were observed when mAb-**1** is directly fluoridated on streptavidin-agarose (4.9 mCi/μmol is obtained (t = 220 min) (Figure S12)).

DOI: 10.1021/acs.bioconjchem.6b00164
Bioconjugate Chem. 2016, 27, 1390−1399

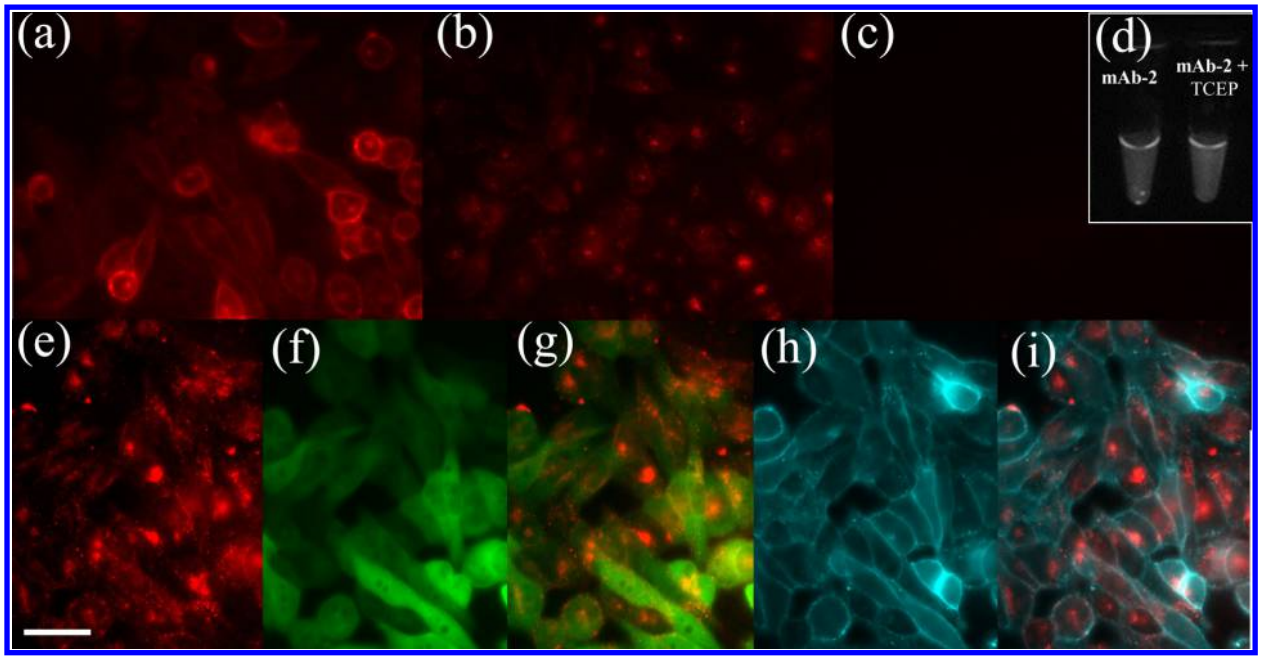

Figure 4. Chemical attachment of mAb to **1**, solid-support immobilization, and reaction with [^{19}F]-fluoride does not affect mAb-**2** EpCAM-antigen binding. (a) Fluorescence of mAb-**2** bound to PC3 cells (30 min incubation) shows membrane localization. (b) (Control 1) Membrane bound mAb-**2** (a) was challenged with 100-fold excess of unlabeled mAb for 1 h. Membrane bound fluorescence is diminished, illustrating that antigen binding is required for membrane labeling. Endocytosed mAb-**2** fluorescence remains visible inside the cells. (c) (Control 2) mAb-**2** was reduced to heavy and light chains with TCEP. Equal fluorescent quantities of the reduced mAb-**2** (mAb-**2** + TCEP), as in (a), was incubated with PC3 cells (30 min incubation). The lack of fluorescence demonstrates that mAb-**2** antigen binding is essential for both membrane and endocytosed fluorescence. mAb-**2** + TCEP is not nonspecifically binding and/or endocytosed in PC3 cells. (d) mAbs (used in (a) and (c)) show equivalent Cy7 fluorescence. (e) mAb-**2** labeled PC3 cells were incubated for 5 h to promote endocytosis. (f) E2-Crimson fluorescence in the cytoplasm and nuclei of PC3 cells. (g) Overlay of mAb-**2** (e) and E2-Crimson (f) fluorescence. (h) DiO (membrane stain) delineating PC3 cell membranes. (i) Overlay of mAb-**2** (e) and membrane fluorescence (h), confirming increased incubation time confers greater endocytosis of mAb-**2**. Scale bar = 50 μm.

This was 13-fold better than obtained when streptavidin-agarose is not employed, i.e., the solid support was not used to remove mAb and mAb-**1** (0.38 mCi/μmol is obtained (t = 220 min) (Figure S10, Scheme S4a)) and 6.4-fold better then when streptavidin-agarose is added to a premixed mAb-**1** [^{18}F]-fluoride solution, i.e., the solid support was not used to remove mAb (Scheme S4b, Figures S11, S13, S14).

mAb-2 Generation Does Not Alter in Vitro mAb Binding. During a multistep synthesis and purification, a mAb can be denatured and/or chemically modified to eliminate antigen binding. For mAb-**2** to be useful for imaging, mAb antigen-binding must be preserved in all steps of the radiosynthetic scheme, including NHS-ester reaction of **1** with mAb, mAb-**1** immobilization on streptavidin-agarose, fluoride-triggered release of mAb-**2**, and SEC HPLC purification (Scheme S1). Antigen binding is verified by the addition of [^{19}F]-mAb-**2** or >24-h-old [^{18}F]-mAb-**2** to prostate cancer (PC3) cells (Figure 4). Epifluorescence microscopy verifies [^{19}F]-mAb-**2** labeling of PC3 cell membranes (Figure 4a). To show that fluorescence is antigen specific, [^{19}F]-mAb-**2** was prebound to PC3 cells (Figure 4a) and membrane bound [^{19}F]-mAb-**2** was competed off with 100-fold excess of unlabeled mAb. Lack of membrane fluorescence verifies that [^{19}F]-mAb-**2** membrane binding is antigen specific (Figure 4b). Intracellular fluorescence represents endocytosis of [^{19}F]-mAb-**2** bound EpCAM, which is inaccessible to mAb. To verify that antigen binding is required for endocytosis and is not nonspecific cell penetration and/or uptake, [^{19}F]-mAb-**2** was reduced to heavy and light chains using tris(2-carboxyethyl)phosphine (TCEP) (Figure S15). Membrane or internalized fluorescence is not seen with reduced [^{19}F]-mAb-**2** (Figure 4c,d), illustrating that [^{19}F]-mAb-**2** antigen-binding is necessary for endocytosed fluorescence.

Increasing incubation to 5 h, increases [^{19}F]-mAb-**2** endocytosis (Figure 4e). Internalization is verified with [^{19}F]-mAb-**2** colocalization with cytoplasmically expressed red fluorescent protein (RFP) (Figure 4f,g) and lack of localization to DiO membrane dye (Figure 4h,i).

[^{19}F]-mAb-2 Is Viable for Short Time Points in Vivo Fluorescence Imaging. Mice were inoculated with PC3 cells expressing DsRed2 in their left flank and grown to a diameter of 0.5 cm (Figure 5a). [^{19}F]-mAb-**2** was injected intravenously (i.v.) through the tail vein and mice were imaged 6 and 48 h later. [^{19}F]-mAb-**2** fluorescence colocalizes with primary PC3 tumor expressing DsRed2 (Figure 5b,c) and is visible at 6 and 48 h. DsRed2 fluorescence is visible in the primary tumor and metastasizes to the stomach (Figure 5b,iii). [^{19}F]-mAb-**2** fluorescence is brightest on stomach metastases, but visible on the primary tumor (Figure 5c,iii). Colocalization of [^{19}F]-mAb-**2** and DsRed2 fluorescence confirms antigen-binding in vivo and [^{19}F]-mAb-**2** fluorescence is visible on the tumor after 6 h (Figure 5c,i). Fluorescence contrast increases with extended time (24, 48, and 72 h). [^{19}F]-mAb-**2** detection of metastasis was further investigated. Mice were injected with PC3 cells expressing DsRed2 in the upper left breast area and grown to a diameter of 0.5 cm (Figure S16). mAb-**2** was injected i.v. and observed in the primary and subcutaneous metastatic tumors (lower left quadrant of the mouse, Figure S16c,i). When [^{19}F]-mAb-**2** is denatured no fluorescence is seen in the tumor (Figure S16c,ii), confirming that antigen binding is required for

DOI: 10.1021/acs.bioconjchem.6b00164
Bioconjugate Chem. 2016, 27, 1390−1399

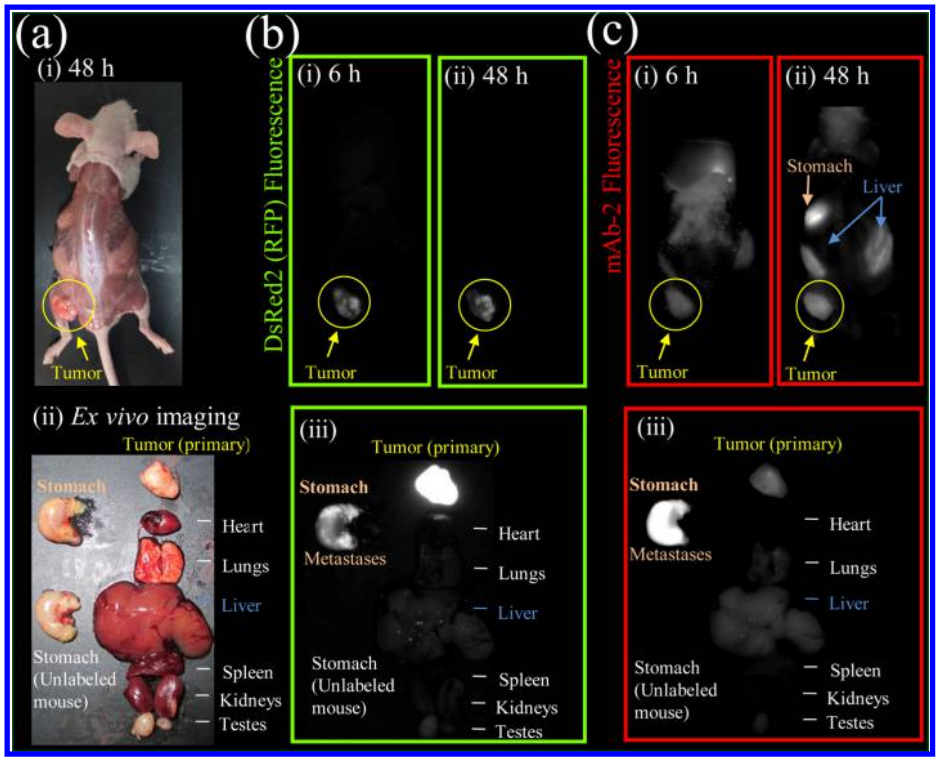

Figure 5. mAb-**2** fluorescence imaging in mice bearing PC3-DsRed2 tumor xenografts, which target both primary and metastatic tumors. (a) Brightfield image of mouse with primary PC3-DsRed2 tumor and stomach metastases (i) without skin and (ii) removed organs. (b) DsRed2 fluorescence of PC3-DsRed2 tumors in mice (i) 6 and (ii) 48 h post mAb-**2** injection, and (iii) ex vivo imaging of organs (48 h). Note in (iii), DsRed2 fluorescence was overexposed to visualize stomach metastases. (c) mAb-**2** (600 pmol) fluorescence imaging at (i) 6 and (ii) 48 h post injection, and (iii) ex vivo imaging of organs (48 h). DsRed2 and mAb-**2** fluorescence colocalize in the primary and metastatic tumors. DsRed2 and Cy7 fluorescence is not visible in the stomach of mice without PC3-DsRed2 tumors or mAb-**2** (see control organ in bottom left (b,iii) and (c,iii)).

tumor fluorescence and enhanced permeability and retention (EPR) of the tumor is not causing fluorescence.

Eluted [^{19}F]-Cetuximab-2 Binds A549 Cells. Cetuximab-**1** treatment with fluoride releases [^{19}F]-Cetuximab-**2**, which was tested for EGFR binding on the surface of A549 cells by flow cytometry. Cetuximab-**1** was treated with mixtures of 0−2000 mM HF and 0−111 mM HCl (<pH 3). mAb-**1** (anti-EpCAM) is a control because A549 cells have low surface expression of EpCAM.[30] Fluoride treated Cetuximab-**1**/**2** show cyanine7 fluorescence on A549 cells, which is greater than mAb-**1** fluorescence (Figure S17). Cetuximab-**1**/**2** binding to A549 cells is verified by a secondary Ab conjugated to phycoerythrin (Figure 6). Cetuximab-**1** treated with fluoride and PBS neutralization does not inhibit [^{19}F]-Cetuximab-**2** EGFR recognition on A549 cells.

[^{18}F]-Cetuximab-2 Images A549 Lung Tumors in Vivo. [^{18}F]-PET imaging was performed on orthotopic A549 lung tumors. The orthotopic lung tumor model is a challenging model for PET imaging as the lung is a low density structure that is better imaged with a low positron-energy emitter, like ^{18}F. The tumor is located close to many tissues with high contrast content. There are two major advantages to choosing a orthotopic lung model over the standard subcutaneous flank model: (1) the biology of the xenographed tissue is more representative to that of its target tissue, and (2) orthotopic A549 tumors reliably metastasize into the lung, unlike PC3 subcutaneous tumors that metastasize unpredictably. Eight mice were inoculated with A549 cells expressing luciferase and GFP by transpleural injection through the left rib cage. Bioluminescence imaging was used to verify a chest-wall, primary tumor, which is also visible by CT (0.5 cm diameter, Figure 6a,b). [^{18}F]-Cetuximab-**2** (70 mCi/μmol) was injected i.v. through the tail vein. PET imaging for 1 h with [^{18}F]-Cetuximab-**2** at 1.5 (n = 3) and 4.5 (n = 4) hours shows signal at the primary tumor (Figure 6c). PET signal and A549 metastases in multiple lobes of the lung are observed (Figure S18) and were verified by post-PET dissection (Figure S18e). Mice were sacrificed after PET scanning (2.5 (n = 3) or 6 (n = 4) hours). Removed organs (Figure 6d) were fluorescently imaged for GFP (Figure 6e) and Cy7 labeled Cetuximab-**2** (Figure 6f). Cetuximab-**2**, Cy7 fluorescence is visible in the primary and metastatic lung tumors but is heterogeneously distributed. Heterogeneous A549 GFP expression is confirmed on high-magnification fluorescence histology (Figure 6i,j). These local, nonhomogeneous distributions complicate the reconciliation of whole organ scintillated biodistribution with the high-resolution fluorescent Cetuximab-**2** data. Nevertheless, standard scintillation and ROI analyses (%ID/g in Figure 6g and %ID in Figures S19, S20) show significant difference between [^{18}F]-Cetuximab-**2** in the primary, chest wall tumor and the lung, suggesting that A549 tumor is distinguishable after 6 h by [^{18}F]-PET (P = 0.043). [^{18}F]-Cetuximab-**2** is reduced in metastases to the lung because there is a mixture of normal and cancer cells (Figure 6e,j, Figure S18c−e). [^{18}F]-Cetuximab-**2** signal is present in the heart and spleen because of the long half-life in the blood. These signals decrease over time.[31,32] This experiment demonstrates that the utility of NIRF fluorescence as fluorescent organs, tissues, and single cells can be visualized after [^{18}F]-PET imaging. Most significantly, the direct fluoridation of a boronate-bearing mAb is demonstrated and [^{18}F]-Cetuximab-**2** is generated in quantities that are large

DOI: 10.1021/acs.bioconjchem.6b00164
Bioconjugate Chem. 2016, 27, 1390−1399

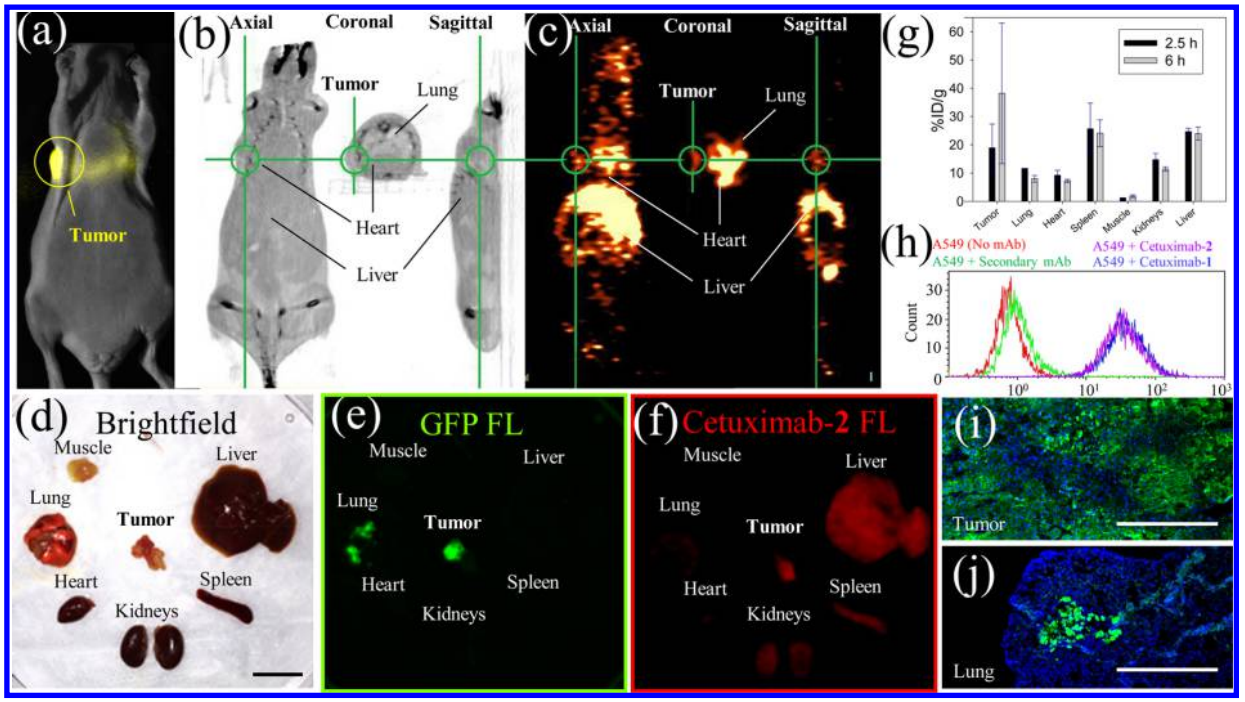

Figure 6. [^{18}F]-Cetuximab-**2** imaging in mice bearing orthotopic A549 tumor xenografts expressing luciferase and GFP. (a) Bioluminescent imaging of A549 orthotopic lung tumor xenograft shows primary tumor above the lung. (b,c) Axial, coronal, and sagittal [^{18}F]-Cetuximab-**2** CT (b) and PET (c) cross-sectional images of the primary tumor (green circle) 4.5 h after i.v. injection. (d) Excised organs following PET imaging. Scale bar = 1 cm. (e) Fluorescent imaging of primary and lung metastatic tumors expressing GFP. (f) NIRF imaging of Cy7 labeled Cetuximab-**2**, verifying colocalization of GFP and Cetuximab-**2** to primary and lung metastatic tumors. (g) Scintillated biodistribution (obtained after ex vivo imaging) at 2.5 (n = 3) and 6 h (n = 4). Error bars = SEM (h) Secondary Ab-phycoerythrin labeling of Cetuximab-**1** and Cetuximab-**2**. Flow cytometry demonstrates that Cetuximab-**1** treated with [^{18}F]-fluoride binds EGFR expressed on A549 cells. (i,j) Fluorescent imaging of A549 cells expressing GFP in tissue slices from (e) showing a heterogeneous GFP expression (i) and metastatic invasion into the lung (j). GFP is green, DAPI (nuclear stain) is blue, and scale bar = 400 μm.

enough for multiple animal imaging (Videos S1,S2), allowing us to consider advanced antibody imaging studies in more than seven mice from a single, 150 mCi dose of evaporated [^{18}F]-fluoride ion activity.

DISCUSSION

A bioorthogonal method for specific, covalent bond cleavage using inert fluoride ion is described. Boron-based fluoride capture allows the radiolabeling of mAbs without organic solvents and/or high temperatures. This treatment does not affect mAb-antigen affinity as verified by fluorescence microscopy and fluorescence assisted cell counting. Immobilization of mAb-**1** to streptavidin-agarose, solid phase allows for direct fluoridation that simultaneously generates [^{18}F]-mAb-**2**, a [^{18}F]-PET/NIRF multimodality imaging probe, and facilitates its removal from mAb and mAb-**1** (Scheme S1). The radiosynthesis of [^{18}F]-mAb-**2** (160 mCi/μmol) is comparable to that reported with [^{18}F]-fluorobenzoate-diabody (~50 mCi/μmol).[33] In our hands, this was sufficient for imaging seven mice simultaneously. If desired, larger activities could be achieved by starting with greater [^{18}F]-activities of ^{18}F (2 Ci) or by reformulating synthon **iii** (Scheme S2) as alkyl boronates.[6] Alternatively, this technology was designed with aqueous electrowetting dielectric microfluidic (EWOD) compatibility in mind.[34] EWOD can generate specific activities upward of 20 Ci/μmol on a small molecule starting from just 8 mCi of activity.[34] Higher specific activities may limit fluorescent visibility on PET/FL probes.[35,36]

Previous strategies for generating ^{18}F-mAbs require multiple synthetic steps; solvent/phase transfers, large activities, robotic manipulation, and automation that must be performed in the face of rapid ^{18}F-precursor decay. The chemistry described here is unique, as enough ^{18}F labeled mAb activity is generated for a comprehensive ^{18}F-mAb analysis in seven mice. This is the second study to demonstrate the in vivo imaging of a ^{18}F-PET/FL-mAb.[15] The chemistry described here is achieved without the use of organic cosolvents or higher temperatures, making this labeling strategy ideally compatible with antibodies, biological molecules, and holocomplexes, agents that are particularly sensitive to precipitation and denaturation when heated or exposed to organic solvents. This strategy also incorporates ^{18}F in a final step, allowing one to save valuable time by avoiding the purification of preconjugates. The sulfonated heptamethine cyanine, and biotinylated precursor **1**, was deliberately designed to be more water-soluble than maleimidyl, DBCO-click, and inverse electron demand Diels-Alder (tetrazine) pretargeting systems. This is advantageous, as cosolvents that are required to solubilize these chemistries can denature or inactivate complex biomolecules.

Cetuximab is clinically relevant, and is inexpensive relative to mAb fragments for developing new radiochemistry. There are many literature reports of Cetuximab PET imaging. For these reasons, we found Cetuximab to be more appropriate than small molecules or reengineered mAbs as a surrogate for demonstrating biocompatible dioxaborolane chemistry. We note that the choice to image a systemic mAb is not ideal (in a clinical, systemic application), as the half-life of fluoride-18 (110 min) and mAb biodistribution (>12 h) do not match prima facie.[31,32] Conventional thinking suggests that fluoride-18 is more suited for imaging diabodies and antibody fragments,

DOI: 10.1021/acs.bioconjchem.6b00164
Bioconjugate Chem. 2016, 27, 1390−1399

agents with pharmacokinetic distribution half-lives similar to the half-lives of isotope decay. Matching half-life with biomolecular biodistribution allows maximization of signal-to-noise when imaging a tumor. At the onset of this project we initially attempted to isolate pure, single-band [^{18}F]-PET/NIRF labeled Fab fragments (with Pierce Fab Preparation kit #44985) and diabodies for [^{18}F]-PET/NIRF imaging. This was difficult and cost prohibitive because gel purification of low-molecular-weight fragments was low yielding and 20 mg of Cetuximab was utilized to complete this entire project.

Alternatively, a mAb that is reengineered will not accurately represent the distribution and clearance of its therapeutic, clinical mAb counterpart. This is problematic if one wished to use the fluorescence component of a PET/NIRF mAb fragment to image (1) antigen binding and endocytosis in histology; (2) homogeneous mAb distribution to antigen expressing cells/distribution of a mAb therapeutic to the margins of a tumor; or (3) striated or streamlined routes of mAb clearance that may minimize distribution of a mAb drug to a tumor (and would counterproductively encourage chemoresistance). For these situations one may consider a third alternative; the ^{89}Zr-PET/NIRF labeled mAb. Unfortunately, the drawback to PET imaging is that multiple radioactive isotope labeled antibodies cannot be imaged in parallel, and one must wait for individual isotope decay before a second radioactive isotope labeled antibody is imaged. This is relevant in imaging intratumoral heterogeneity[37] (Figure 6d−j), where a tumor may respond to two or more mAb therapies. Awaiting isotope decay can translate into weeks between ^{89}Zr scans, which is prohibitive in imaging a fast-growing tumor. Given these caveats, one may wish to consider a [^{18}F]-PET/NIRF-mAb, where a short-lived PET isotope would rapidly decay, allowing the prompt, next day imaging of another antibody.

Reduction in radioactive signal for PET imaging over time is problematic, but is compensated by the use of fluorophores (FLs), which retain fluorescence imaging capability far beyond the temporal window of radioactive isotope decay. Additionally, PET/FL probes can be screened in parallel using different antibodies labeled with multiple, spectrally distinct fluorophores for simultaneous imaging of multiple antigens. Unfortunately, the in vivo fluorescence quantification of a [^{18}F]-PET/NIRF-mAb would require fluorescent endoscopy. This is debatably less invasive than the PET radiation incurred from multiple back-to-back ^{89}Zr antibody scans, but would accurately predict in vivo distributions of therapeutic antibodies like Erbitux. NIRF imaging of antigen-positive tumor resections (Figure 6) is used to corroborate in vivo PET imaging, and NIRF is capable of spatial resolution (Figure 4) that greatly exceeds that of PET.[15] The ability to image heterogeneity in tumor histology, even after quantitative [^{18}F]-isotope decay,[7] adds another dimension to PET/NIRF imaging that cannot be observed with the inferior resolution of PET scintillated biodistribution alone.

The successful transformation of an antibody into a multimodality imaging agent highlights this technology's clear, nondenaturing potential on contrast agents with current, therapeutic utility.[38−40] This technology is not limited to systemic mAbs injections, and sets a precedent for the conjugation of **1** and Mal-**1** to amine and thiol containing agents, respectively, including commercially available Abs, diabodies,[41−43] nanobodies, nanoparticles, and small molecules for the dual modality imaging of a vast number of cancer biomarkers and disease-related proteins to many human maladies.

EXPERIMENTAL PROCEDURES

mAb/Cetuximab Labeling with the Boronate/NIRF Probe, 1. **1** (1 μL, 2100 pmol, 2.1 mM in DMSO) was added to 62.5 μL of a 20 μM mAb solution (1250 pmol, EpCAM/TROP1 mAb (Clone 158206, R&D systems, MAB9601) or Erbitux (Cetuximab, ImClone). Amide bond formation was initiated with 2.6 μL of 910 mM *N*-methylmorpholine (NMM) with total volume of 66.1 μL containing 31.8 μM **1**, 18.9 μM mAb, and 35.8 mM NMM for 1 h. Absorbance based quantification gave 1−2 molecules of Cy7 per mAb. mAb-**1**/Cetuximab-**1** synthesis was verified by SEC HPLC on a Shodex 802.5, 400 Å, 300 cm × 8.0 mm silica hydrophilic polymer column (F6989000) using an isocratic solution of 250 mM PBS (pH 7.5) and a flow rate of 1 mL/min mAb-**1**/Cetuximab-**1** elutes between 5 and 7 min mAb-**1**/Cetuximab-**1** labeling was also verified by PAGE (Figure 2). mAb-**1**/Cetuximab-**1** is visible by Cy7 fluorescence (CRI Maestro full field fluorescence imager; excitation/emission of 730(42)/800LP).

Solid-Phase mAb-1/Cetuximab-1 [$^{18/19}$F]-Generator Construction. 19.5 μL of mAb-**1**/Cetuximab-**1** (372 pmol) was added to 30 μL streptavidin-agarose (Solulink, N-1000-005) and incubated for 5 min. The mixture was transferred to a Spin-X 0.22 μm cellulose acetate filter (Costar, 8161) or a microspin column (30 μm polyethylene filter, Thermo Scientific, 89879) and was centrifuged at 4000 rcf for 1 min. The filtrate was discarded and streptavidin-agarose was resuspended in 500 μL of diH_2O. The streptavidin-agarose was washed 3× 500 μL diH_2O to completely remove unconjugated mAb and PBS buffer from mAb-**1**/Cetuximab-**1**.

Fluoride-Triggered mAb-2 Release from Streptavidin-Agarose. Dry, mAb-**1**/Cetuximab-**1**-bound streptavidin-agarose was resuspended in 70 μL of diH_2O, and distributed into 12, 5 μL aliquots to microspin columns (Thermo Scientific Pierce). HF (concentrations listed in Figure 2) was added to the microspin columns to give a final volume of 15 μL (pH 3). Fluoridation proceeded for 15 min and reactions were quenched with 10 μL of 1 M PBS (pH 7.4). Microspin columns were centrifuged at 4000 rcf for 1 min to elute mAb-**2**/Cetuximab-**2**, which was analyzed by SEC HPLC or PAGE.

Solid-Phase, [^{18}F]-Fluoride Radiolabeling of mAb-1/Cetuximab-1 and [^{18}F]-mAb-2/Cetuximab-2 Elution. Radioactive work must be done with proper institutional approval and oversight, and ALARA precautions. Dry, mAb-**1**/Cetuximab-**1**-bound streptavidin-agarose (1200 pmols mAb) in 30 μm polyethylene filtered microspin columns were resuspended in 4 μL of a 29.3 mCi [^{18}F]-fluoride solution (PETNET, time of reaction (TOR) = 0 min), containing 1.5 μL of 1 M HCl, and 1.5 μL of 37 mM [^{19}F]-carrier hydrogen fluoride (pH 2−3, final volume 15 μL, HCl is required to quench buffer that is introduced by the mAb and solulink). Room temperature nitrogen flow was passed over the streptavidin-agarose as fluoridation proceeded for 69 min (TOR = 69 min) before 50 μL of 250 mM PBS (pH 6.5) was added to neutralize. The microspin column containing [^{18}F]-mAb-**2**/Cetuximab-**2** was centrifuged to elute radiolabeled [^{18}F]-mAb-**2**/Cetuximab-**2**, which was chromatographed by SEC HPLC using an isocratic 25 mM PBS (pH 6.5) and 200 mM NaCl solution as an eluent ([^{18}F]-mAb-**2**/Cetuximab-**2** was purified with 250 mM PBS solution 0 mM NaCl (pH 6.5)). [^{18}F]-mAb-**2**/Cetuximab-**2** elutes between 5 and 7 min, in a fraction containing both [^{18}F]-activity and Cy7 fluorescence.

DOI: 10.1021/acs.bioconjchem.6b00164
Bioconjugate Chem. 2016, 27, 1390−1399

[^{18}F]-mAb-**2**/Cetuximab-**2** can be injected into mice immediately following elution.

In Vitro Cell Imaging with mAb-2. PC3 cells in DMEM (Corning, 10-014-CV) and A549 cells in RPMI 1640 (Gibco, 11875) were grown in 10% FBS (Atlanta Biological, S11150) + 1 × penicillin-streptomycin (Fisher Sci., SV30010) growth media on poly(D-lysine) coated glass bottom culture dishes (MatTek, P35G-0-14-C). mAb-**2**/mAb/mAb-**2** + TCEP labeling was done in growth medium with incubation times listed in Figure 4. Unbound mAb-**2**/mAb/mAb-**2** + TCEP was removed by washing 2 × 2 mL of growth medium and 2 × 2 mL 1× Hank's balanced salt solution (HBSS, Life Technologies, 14065-056) + 2 g/L glucose + 20 mM HEPES (pH 7.4). Fluorescent images were taken on a Zeiss Axiovert 200 M inverted microscope controlled by SlideBook software. Dyes/FPs were imaged with the following settings: DIO excitation/emission of 495(10)/535(25) nm, respectively. DsRed2 excitation/emission of 540(25)/595(50) nm, respectively. E2-Crimson excitation/emission of 628(40)/680(30) nm, respectively. Cy7 excitation/emission of 710(40)/785(62) nm, respectively.

Animal Imaging. All procedures conducted in mice have been approved by UCSD (#S04011) and WCMC (#2014-0007 and #2014-0030) IACUC and are consistent with the recommendations of the AVMA and the NIH Guide for the Care and Use of Laboratory Animals.

In Vivo Fluorescent Imaging of Tumors and Metastases Using mAb-2. 1.5 million PC3 cells were mixed with Corning matrigel matrix (4 mg/mL final concentration) in a total volume of 40 μL. This 40 μL mixture was injected subcutaneously into the lateral, dorsal, lower left flank of athymic nude mice. Tumors were grown for 16 weeks (diameter = 0.5 cm). Mice were anesthetized with 2% isoflurane at a 2 L/min flow and mAb-**2** (90 μg, 600 pmols) was introduced through an i.v. tail vein injection. Isoflurane anesthetized mice on a heated pad were imaged at multiple time points (Figure 6, Figures S18, S19) using a CRI Maestro in vivo, full field fluorescence imaging device. FP/dye was imaged with the following filters: DsRed2 excitation/emission of 530(52)/580LP nm, respectively, and liquid crystal = 590 nm. Cy7 was imaged using an excitation/emission of 730(42)/800LP nm and liquid crystal = 810 nm.

In Vivo PET/NIRF Imaging and Scintillation of Primary and Metastatic Tumors Using [^{18}F]-Cetuximab-2. Animals were anesthetized with 2% isoflurane and placed in a lateral decubitus position. Two million A549 cells expressing luciferase and GFP (35 μL) were mixed with 35 μL matrigel and then directly injected into the chest wall/pleural cavity to a depth of 6 mm using a 25 G needle through the intercostal space on the left rib cage below the clavicle and just right of the left anterior axillary line. Mice were placed on a heating pad until recovered. Tumors were grown for 5 weeks (diameter = 0.5 cm). Mice were anesthetized with 2% isoflurane and [^{18}F]-Cetuximab-**2** (25−100 μCi, 10 μg/mouse) was introduced through an i.v. tail vein injection. Mice were fixed on trays such that up to four mice could be imaged simultaneously along with a 200 mL flask containing ∼40 °C water in a Siemen's Inveon PET/CT. A 10 min CT scan and a 60 min PET scan was acquired 1.5 and 4.5 h following injection. Biodistribution was performed at 2.5 (n = 3) or 6 (n = 4) hours post injection. PET/CT were processed with Amide v 1.0.4 and Inveon Research Workplace. Mice were sacrificed by cervical dislocation and tissues were collected and weighed for macroscopic imaging, scintigraphy, and histological sectioning. Fluorescent organ imaging was performed on Petri dishes immediately following PET/CT scanning using a Bruker Xtreme full field fluorescence imaging device. Tissue containing A549 expressing GFP was imaged with excitation/emission of 486/535 nm, respectively, and Cy7 Cetuximab-**2** was imaged with excitation/emission of 730/790 nm, respectively. Tissues were transferred to test tubes that were scintillated on a Wallac Wizard 3.0 gamma counter. Following scintillation, tissues were frozen in Optimal Cutting Temperature (OCT) Compound (Sakura Tissue-Tec, #4585) cryogenic embedding medium and analyzed by cryohistology on an Axiovert 200 fluorescent microscope.

■ ASSOCIATED CONTENT

Supporting Information

The Supporting Information is available free of charge on the ACS Publications website at DOI: 10.1021/acs.bioconjchem.6b00164.

Experimental Procedures. Scheme S1. Generation of a mAb-**1** bound to streptavidin-agarose and radioactive fluoride triggered release of mAb-**2**. Scheme S2. Synthesis of a boronated, [$^{18/19}$F]-PET/NIRF precursor, **1**, modified with a biotin. Scheme S3. Fluoride treatment of **1** frees biotinylated pinacol from the [^{18}F]-PET/NIRF probe, **2**, via trifluoroborate formation. Scheme S4. Three different syntheses of [^{18}F]-mAb-**2** to monitor the effect of streptavidin-agarose on specific activity. Figure S1. Mal-**1** synthesis and aqueous conversion into the trifluoroborate, Mal-**2**. Figure S2. Reactions of Mal-**1** with various concentrations of fluoride. Figure S3. Fluorescence imaging of Mal-**1**-biotin capture on magnetic streptavidin-IO (str-IO) particles (pH 7.4). Figure S4. Fluoride triggered elution of Mal-**2** from Mal-**1** bound streptavidin-agarose. Figure S5. SEC HPLC analyses of mAb and mAb-**1**. Figure S6. PAGE gel demonstrates mAb-**1** binding to streptavidin-agarose. Figure S7. Coomassie stained gel demonstrating the lack of nonspecific binding between unreacted mAb and streptavidin-agarose. Figure S8. HPLC confirmation of the quantitative conversion of **1** into its trifluoroborate, **2**. Figure S9. SDS-PAGE gel of mAb-**2** demonstrating a lack of binding between 37 pmols mAb-**2** and streptavidin-agarose. Figure S10. SEC HPLC elution profile of mAb-**1** reacted at room temperature for 130 min with aqueous [^{18}F]-fluoride. Figure S11. SEC HPLC analysis of the supernatant resulting from the reaction of mAb-**1** with aqueous [^{18}F]-fluoride, followed by a work up with streptavidin-agarose. Figure S12. SEC HPLC analysis of the eluent generated from mAb-**1** bound to streptavidin-agarose reacted with [^{18}F]-fluoride. Figure S13. SEC HPLC analysis demonstrating the lack of non-specific binding/labeling between unmodified mAb and [^{18}F]-fluoride. Figure S14. Comparison of relative specific activities for different preparations of mAb-**2**. Figure S15. SDS PAGE gel of the chemical reduction of mAb-**2** into fragments. Figure S16. Viable and heat-denatured mAb-**2** imaging of PC3-DsRed2 tumor xenografts in mice. Figure S17. Flow cytometry analysis of Cetuximab-**1**/**2** binding to EGFR expressed on A549 cells after various fluoridation concentrations (pH 3). Figure S18. A549 primary and metastatic lung tumor confirmation and lung focused PET/CT. Figure S19. Tumor focused PET/CT imaging and tissue biodistribution data confirming [^{18}F]-Cetuximab-**2** signal in

DOI: 10.1021/acs.bioconjchem.6b00164
Bioconjugate Chem. 2016, 27, 1390−1399

orthotopic A549 tumor. Figure S20. ROI analyses of mice in Figure 6g. (PDF)

Video S1. Sample PET/CT scan of [^{18}F]-Cetuximab-**2** dosing study in four mice bearing immature A549 lung tumors. (AVI)

Video S2. PET scan of [^{18}F]-Herceptin-**2** in four mice bearing immature A549 lung tumors prepared using the Cetuximab labeling procedure. (AVI)

AUTHOR INFORMATION

Corresponding Author

*E-mail: rct2001@med.cornell.edu. Tel: 6469626195. Fax: 6469620577.

Author Contributions

#E.A.R and Y.W. contributed equally to this work.

Notes

The authors declare no competing financial interest.

ACKNOWLEDGMENTS

We thank L. Gross for obtaining high-resolution mass spectrometry data. E.A.R. was funded by the National Institute of General Medical Sciences Postdoctoral Fellowship (F32GM089114). The project is supported by grants to R.Y.T. from the US National Institutes of Health (CA158448) and the Howard Hughes Medical Institute. R.T. is funded by the National Institute of Biomedical Imaging and Bioengineering K99/R00 (EB013904).

REFERENCES

(1) Lippert, A. R., Van de Bittner, G. C., and Chang, C. J. (2011) Boronate oxidation as a bioorthogonal reaction approach for studying the chemistry of hydrogen peroxide in living systems. *Acc. Chem. Res. 44*, 793−804.

(2) Miller, E. W., Albers, A. E., Pralle, A., Isacoff, E. Y., and Chang, C. J. (2005) Boronate-based fluorescent probes for imaging cellular hydrogen peroxide. *J. Am. Chem. Soc. 127*, 16652−16659.

(3) Chang, M. C., Pralle, A., Isacoff, E. Y., and Chang, C. J. (2004) A selective, cell-permeable optical probe for hydrogen peroxide in living cells. *J. Am. Chem. Soc. 126*, 15392−15393.

(4) Ting, R., Adam, M. J., Ruth, T. J., and Perrin, D. M. (2005) Arylfluoroborates and alkylfluorosilicates as potential PET imaging agents: high-yielding aqueous biomolecular ^{18}F-labeling. *J. Am. Chem. Soc. 127*, 13094−13095.

(5) Ting, R., Harwig, C., auf dem Keller, U., McCormick, S., Austin, P., Overall, C. M., Adam, M. J., Ruth, T. J., and Perrin, D. M. (2008) Toward [^{18}F]-labeled aryltrifluoroborate radiotracers: *in vivo* positron emission tomography imaging of stable aryltrifluoroborate clearance in mice. *J. Am. Chem. Soc. 130*, 12045−12055.

(6) Liu, Z. B., Pourghiasian, M., Radtke, M. A., Lau, J., Pan, J. H., Dias, G. M., Yapp, D., Lin, K. S., Benard, F., and Perrin, D. M. (2014) An organotrifluoroborate for broadly applicable one-step ^{18}F-labeling. *Angew. Chem., Int. Ed. 53*, 11876−11880.

(7) Ting, R., Aguilera, T. A., Crisp, J. L., Hall, D. J., Eckelman, W. C., Vera, D. R., and Tsien, R. Y. (2010) Fast ^{18}F labeling of a near-infrared fluorophore enables positron emission tomography and optical imaging of sentinel lymph nodes. *Bioconjugate Chem. 21*, 1811−1819.

(8) Lin, W. C., and Morton, T. H. (1991) Two-step affinity chromatography. Model systems and an example using biotin-avidin binding and a fluoridolyzable linker. *J. Org. Chem. 56*, 6850−6856.

(9) Fang, S., and Fueangfung, S. (2010) Scalable synthetic oligodeoxynucleotide purification with use of a catching by polymerization, washing, and releasing approach. *Org. Lett. 12*, 3720−3723.

(10) Leriche, G., Chisholm, L., and Wagner, A. (2012) Cleavable linkers in chemical biology. *Bioorg. Med. Chem. 20*, 571−582.

(11) Liu, Z., Li, Y., Lozada, J., Wong, M. Q., Greene, J., Lin, K. S., Yapp, D., and Perrin, D. M. (2013) Kit-like ^{18}F-labeling of RGD-^{19}F-arytrifluroborate in high yield and at extraordinarily high specific activity with preliminary in vivo tumor imaging. *Nucl. Med. Biol. 40*, 841−849.

(12) Reiserer, A., Ritter, S., and Rempe, G. (2013) Nondestructive detection of an optical photon. *Science 342*, 1349−1351.

(13) Watson, D. A., Su, M., Teverovskiy, G., Zhang, Y., Garcia-Fortanet, J., Kinzel, T., and Buchwald, S. L. (2009) Formation of ArF from LPdAr(F): catalytic conversion of aryl triflates to aryl fluorides. *Science 325*, 1661−1664.

(14) Liu, S., Li, D., Shan, H., Gabbai, F. P., Li, Z., and Conti, P. S. (2014) Evaluation of ^{18}F-labeled BODIPY dye as potential PET agents for myocardial perfusion imaging. *Nucl. Med. Biol. 41*, 120−126.

(15) Hendricks, J. A., Keliher, E. J., Wan, D., Hilderbrand, S. A., Weissleder, R., and Mazitschek, R. (2012) Synthesis of [^{18}F]BODIPY: bifunctional reporter for hybrid optical/positron emission tomography imaging. *Angew. Chem., Int. Ed. 51*, 4603−4606.

(16) Laverman, P., McBride, W. J., Sharkey, R. M., Goldenberg, D. M., and Boerman, O. C. (2014) Al^{18}F labeling of peptides and proteins. *J. Labelled Compd. Radiopharm. 57*, 219−223.

(17) McBride, W. J., Sharkey, R. M., Karacay, H., D'Souza, C. A., Rossi, E. A., Laverman, P., Chang, C.-H., Boerman, O. C., and Goldenberg, D. M. (2009) A novel method of ^{18}F radiolabeling for PET. *J. Nucl. Med. 50*, 991−998.

(18) Lindner, S., Michler, C., Leidner, S., Rensch, C., Wangler, C., Schirrmacher, R., Bartenstein, P., and Wangler, B. (2014) Synthesis and *in vitro* and *in vivo* evaluation of SiFA-tagged bombesin and RGD peptides as tumor imaging probes for positron emission tomography. *Bioconjugate Chem. 25*, 738−749.

(19) Zhu, J., Chin, J., Wangler, C., Wangler, B., Lennox, R. B., and Schirrmacher, R. (2014) Rapid F-labeling and loading of PEGylated gold nanoparticles for *in vivo* applications. *Bioconjugate Chem. 25*, 1143−1150.

(20) Tsien, R. Y. (2003) Imagining imaging's future. *Nat. Rev. Mol. Cell Biol. Suppl.*, SS16−21.

(21) Lütje, S., Rijpkema, M., Helfrich, W., Oyen, W. J. G., and Boerman, O. C. (2014) Targeted radionuclide and fluorescence dual-modality imaging of cancer: Preclinical advances and clinical translation. *Mol. Imaging Biol. 16*, 747−755.

(22) Sevick-Muraca, E. M., Kwon, S., and Rasmussen, J. C. (2014) Emerging lymphatic imaging technologies for mouse and man. *J. Clin. Invest. 124*, 905−914.

(23) Tucker, W. D., Greene, M. W., and Murrenhoff, A. P. (1960) Gewinnung von tragerfreiem Te-132, J-132 und Mo-99 aus neutronenbestrahltem uran durch fraktionierte sorption an aluminiumoxyd. *Zeitschrift Fur Elektrochemie 64*, 1072−1072.

(24) Sutcliffe-Goulden, J. L., O'Doherty, M. J., and Bansal, S. S. (2000) Solid phase synthesis of [^{18}F]labelled peptides for positron emission tomography. *Bioorg. Med. Chem. Lett. 10*, 1501−1503.

(25) Seibold, U., Wangler, B., Schirrmacher, R., and Wangler, C. (2014) Bimodal imaging probes for combined PET and OI: recent developments and future directions for hybrid agent development. *BioMed Res. Int. 2014*, 1−13.

(26) Azhdarinia, A., Ghosh, P., Ghosh, S., Wilganowski, N., and Sevick-Muraca, E. M. (2012) Dual-labeling strategies for nuclear and fluorescence molecular imaging: a review and analysis. *Mol. Imaging Biol. 14*, 261−276.

(27) Lutje, S., Rijpkema, M., Goldenberg, D. M., van Rij, C. M., Sharkey, R. M., McBride, W. J., Franssen, G. M., Frielink, C., Helfrich, W., Oyen, W. J., et al. (2014) Pretargeted dual-modality immuno-SPECT and near-infrared fluorescence imaging for image-guided surgery of prostate cancer. *Cancer Res. 74*, 6216−6223.

(28) Luther, N., Zhou, Z., Zanzonico, P., Cheung, N. K., Humm, J., Edgar, M. A., and Souweidane, M. M. (2014) The potential of theragnostic ^{124}I-8H9 convection-enhanced delivery in diffuse intrinsic pontine glioma. *Neuro. Oncol. 16*, 800−806.

(29) Arigami, T., Natsugoe, S., Uenosono, Y., Arima, H., Mataki, Y., Ehi, K., Yanagida, S., Ishigami, S., Hokita, S., and Aikou, T. (2005)

DOI: 10.1021/acs.bioconjchem.6b00164
Bioconjugate Chem. 2016, 27, 1390−1399

Lymphatic invasion using D2−40 monoclonal antibody and its relationship to lymph node micrometastasis in pN0 gastric cancer. *Br. J. Cancer 93*, 688−693.
(30) Kim, Y., Kim, H. S., Cui, Z. Y., Lee, H. S., Ahn, J. S., Park, C. K., Park, K., and Ahn, M. J. (2009) Clinicopathological implications of EpCAM expression in adenocarcinoma of the lung. *Anticancer Res. 29*, 1817−1822.
(31) Kenanova, V., and Wu, A. M. (2006) Tailoring antibodies for radionuclide delivery. *Expert Opin. Drug Delivery 3*, 53−70.
(32) Vieira, P., and Rajewsky, K. (1988) The half-lives of serum immunoglobulins in adult mice. *Eur. J. Immunol. 18*, 313−316.
(33) Cai, W., Olafsen, T., Zhang, X., Cao, Q., Gambhir, S. S., Williams, L. E., Wu, A. M., and Chen, X. (2007) PET imaging of colorectal cancer in xenograft-bearing mice by use of an ^{18}F-labeled T84.66 anti-carcinoembryonic antigen diabody. *J. Nucl. Med. 48*, 304−310.
(34) Javed, M. R., Chen, S., Lei, J., Collins, J., Sergeev, M., Kim, H. K., Kim, C. J., van Dam, R. M., and Keng, P. Y. (2014) High yield and high specific activity synthesis of [^{18}F]fallypride in a batch microfluidic reactor for micro-PET imaging. *Chem. Commun. (Cambridge, U. K.) 50*, 1192−1194.
(35) Liu, Z. B., Radtke, M. A., Wong, M. Q., Lin, K. S., Yapp, D. T., and Perrin, D. M. (2014) Dual mode fluorescent ^{18}F-PET tracers: Efficient modular synthesis of rhodamine-[cRGD]$_2$-[^{18}F]-organotrifluoroborate, rapid, and high yielding one-step ^{18}F-Labeling at high specific activity, and correlated *in vivo* PET imaging and *ex vivo* fluorescence. *Bioconjugate Chem. 25*, 1951−1962.
(36) Houghton, J. L., Zeglis, B. M., Abdel-Atti, D., Aggeler, R., Sawada, R., Agnew, B. J., Scholz, W. W., and Lewis, J. S. (2015) Site-specifically labeled CA19.9-targeted immunoconjugates for the PET, NIRF, and multimodal PET/NIRF imaging of pancreatic cancer. *Proc. Natl. Acad. Sci. U. S. A. 112*, 15850−15855.
(37) Bedard, P. L., Hansen, A. R., Ratain, M. J., and Siu, L. L. (2013) Tumour heterogeneity in the clinic. *Nature 501*, 355−364.
(38) Tichauer, K. M., Samkoe, K. S., Gunn, J. R., Kanick, S. C., Hoopes, P. J., Barth, R. J., Kaufman, P. A., Hasan, T., and Pogue, B. W. (2014) Microscopic lymph node tumor burden quantified by macroscopic dual-tracer molecular imaging. *Nat. Med. 20*, 1348−1353.
(39) Carter, P. (2001) Improving the efficacy of antibody-based cancer therapies. *Nat. Rev. Cancer 1*, 118−129.
(40) Carter, P. J., and Senter, P. D. (2008) Antibody-drug conjugates for cancer therapy. *Cancer J. 14*, 154−169.
(41) Wu, A. M., Yazaki, P. J., Tsai, S. W., Nguyen, K., Anderson, A. L., McCarthy, D. W., Welch, M. J., Shively, J. E., Williams, L. E., Raubitschek, A. A., et al. (2000) High-resolution microPET imaging of carcino-embryonic antigen-positive xenografts by using a copper-64-labeled engineered antibody fragment. *Proc. Natl. Acad. Sci. U. S. A. 97*, 8495−8500.
(42) Robinson, M. K., Doss, M., Shaller, C., Narayanan, D., Marks, J. D., Adler, L. P., Gonzalez Trotter, D. E., and Adams, G. P. (2005) Quantitative immuno-positron emission tomography imaging of HER2-positive tumor xenografts with an iodine-124 labeled anti-HER2 diabody. *Cancer Res. 65*, 1471−1478.
(43) Nielsen, U. B., Adams, G. P., Weiner, L. M., and Marks, J. D. (2000) Targeting of bivalent anti-ErbB2 diabody antibody fragments to tumor cells is independent of the intrinsic antibody affinity. *Cancer Res. 60*, 6434−6440.

DOI: 10.1021/acs.bioconjchem.6b00164
Bioconjugate Chem. 2016, 27, 1390−1399